

Quantitative modal analysis of optical power flow and energy loss in photonic structures with a dipole emission source

Sujin Choi,¹ Seungin Baek,² Dajeong Im,¹ Hyun Kook Kahng,¹ and Hwi Kim^{1,*}

¹ICT Convergence Technology for Health & Safety, Department of Electronics and Information Engineering, Korea University, 2511 Sejong-ro, Sejong 339-700, South Korea

²Samung Display Co. Ltd., South Korea

*hwikim@korea.ac.kr

Abstract: Fourier modal method based quantitative analysis method of optical power flow and energy loss in general multi-block photonic structures with an internal dipole emitter is described. The analytic expressions of modal power flow and loss are derived for accurate and efficient quantitative analysis. It is revealed that a few dominating excited photonic modes substantially govern the internal energy flow and energy loss. The optical characteristics of the dominant modes are investigated.

©2014 Optical Society of America

OCIS codes: (050.1755) Computational electromagnetic methods; (260.2110) Electromagnetic optics; (080.2710) Inhomogeneous optical media; (120.2040) Displays.

References and links

1. R. Meerheim, M. Furno, S. Hofmann, B. Lüssem, and K. Leo, "Quantification of energy loss mechanisms in organic light-emitting diodes," *Appl. Phys. Lett.* **97**(25), 253305 (2010).
2. S. Nowy, B. C. Krummacher, J. Frischeisen, N. A. Reinke, and W. Brütting, "Light extraction and optical loss mechanisms in organic light-emitting diodes: Influence of the emitter quantum efficiency," *J. Appl. Phys.* **104**(12), 123109 (2008).
3. M. Furno, R. Meerheim, S. Hofmann, B. Lüssem, and K. Leo, "Efficiency and rate of spontaneous emission in organic electroluminescent devices," *Phys. Rev. B* **85**(11), 115205 (2012).
4. M. Furno, T. Rosenow, M. Gather, B. Lüssem, and K. Leo, "Analysis of the external and internal quantum efficiency of multi-emitter, white organic light emitting diodes," *Appl. Phys. Lett.* **101**(14), 143304 (2012).
5. J.-B. Kim, J.-H. Lee, C. K. Moon, S.-Y. Kim, and J.-J. Kim, "Highly enhanced light extraction from surface plasmonic loss minimized organic light-emitting diodes," *Adv. Mater.* **25**(26), 3571–3577 (2013).
6. S. Wooh, H. Yoon, J.-H. Jung, Y.-G. Lee, J. H. Koh, B. Lee, Y. S. Kang, and K. Char, "Efficient light harvesting with micropatterned 3D pyramidal photoanodes in dye-sensitized solar cells," *Adv. Mater.* **25**(22), 3111–3116 (2013).
7. S. Demtsu and J. Sites, "Quantification of losses in thin-film CdS/CdTe solar cells," *Proc. IEEE Photovoltaic Specialists Conf.* **31**, 347–350 (2005).
8. W. Lee, S.-Y. Lee, J. Kim, S. C. Kim, and B. Lee, "A numerical analysis of the effect of partially-coherent light in photovoltaic devices considering coherent length," *Opt. Express* **20**(S6), A941–A953 (2012).
9. S. Lee, S. In, D. R. Mason, and N. Park, "Incorporation of nanovoids into metallic gratings for broadband plasmonic organic solar cells," *Opt. Express* **21**(4), 4055–4060 (2013).
10. Y. Chembo and N. Yu, "Modal expansion approach to optical-frequency-comb generation with monolithic whispering-gallery-mode resonators," *Phys. Rev. A* **82**(3), 033801 (2010).
11. K. Sakoda, *Optical Properties of Photonic Crystals* (Springer, New York, 2004).
12. H. Kim, J. Park, and B. Lee, *Fourier Modal Method and Its Applications in Computational Nanophotonics* (CRC Press, Boca Raton, FL, 2012).
13. L. Novotny and B. Hecht, *Principles of Nano-Optics* (Cambridge University Press, Cambridge, 2006).
14. K. A. Neyts, "Simulation of light emission from thin-film microcavities," *J. Opt. Soc. Am. A* **15**(4), 962–971 (1998).
15. D. N. Chigrin, "Spatial distribution of the emission intensity in a photonic crystal: Self-interference of Bloch eigenwaves," *Phys. Rev. A* **79**(3), 033829 (2009).
16. E. Silberstein, P. Lalanne, J.-P. Hugonin, and Q. Cao, "Use of grating theories in integrated optics," *J. Opt. Soc. Am. A* **18**(11), 2865–2875 (2001).

1. Introduction

The quantitative analysis of optical power flow and energy loss is a fundamental analysis issue for many optical devices [1–9]. The in-depth analysis of external optical power extraction efficiencies and internal losses is crucial to the development of self-radiative optical devices such as light emitting diodes (LEDs) and organic light emitting diodes (OLEDs) [1–5] and optical energy devices such as solar cells [6–9]. To optimize such photonic devices, we need to understand the origin of energy loss and its relation to field distribution.

The modal field analysis methods [10–12] can provide a necessary analysis framework for the modal power and loss quantification. In theory, optical field in general linear photonic structures can be represented by the Bloch eigenmode expansion [11, 12]. The modal field representations inside photonic structures can be used to formulate the modal Poynting vectors by the cross-product form of the modal electric and magnetic fields and produce modal power spectrum. From the modal power spectrum, we can discriminate the contribution ratios of the internal modes to power and loss. In particular, analyzing the photonic modes causing optical loss dominantly allows addressing its origin at the design stage and enhancing the device design strategy in terms of optical efficiency.

In this paper, a Fourier modal method (FMM) [12] based quantitative modal analysis method of optical power flow and energy loss in photonic multi-block structures with internal dipole emitters is proposed. Photonic multi-block structure refers to photonic devices that can be described by cascading multiple blocks with only transversal permittivity variations [12]. In general, conventional OLED, LED, or solar cells can be depicted by the form of multi-block structure. In our analysis, the use of internal dipole emitters is an important point. The internal dipole emitter can be modeled by the classical Weyl representation [13–15]. In Section 2, the FMM model of a dipole radiation in finite multi-block structure is addressed briefly. In Section 3, the computational theory of modal power spectrum is developed. The photonic modes are classified as radiative, leaky, bound and free-space modes and the mathematical representations of their power flow are formulated. The modal power spectrum is visualized and its physical meaning is interpreted in terms of optical efficiency and energy loss. In Section 4, the quantitative energy loss analysis is presented. An example multi-block structure with metal and dielectric blocks is analyzed intensively to elucidate the proposed method. The main goal of the analysis is to understand the modal structure of the optical power flow and energy loss in the given target structure. Concluding remarks are given in Section 5.

2. Optical dipole emission in finite multi-block structure

In this section, mathematical models of optical field and dipole emitter in FMM are briefly described. The optical field distribution excited by a dipole at the origin, $\mathbf{r} = (0, 0, 0)$, is represented by the inhomogeneous Maxwell equations:

$$\nabla \times \mathbf{E} = j\omega\mu_0\mathbf{H}, \quad (1)$$

$$\nabla \times \mathbf{H} = -j\omega\varepsilon_0\varepsilon_r\mathbf{E} - j\omega\mathbf{P}\delta(\mathbf{r}), \quad (2)$$

where \mathbf{P} is the polarization vector of a dipole emitter and ω is the angular frequency of harmonic optical field. ε_0 and μ_0 are permittivity and permeability in free space, respectively. ε_r is the relative permittivity of the homogeneous medium. The time dependent term is assumed to be $\exp(-j\omega t)$. Let us consider a dipole source in homogeneous space with permittivity ε_r . The Green dyadic of the dipole is represented by [13]

$$\tilde{G}^{\pm}(r) = \frac{j\epsilon_r}{2\pi} \int_{k_x} \int_{k_y} \frac{1}{k_z} \begin{pmatrix} 1-p^2 & -pq & \mp pm \\ -qp & 1-q^2 & \mp qm \\ \mp mp & \mp mq & 1-m^2 \end{pmatrix} e^{j(k_x x + k_y y + k_z |z|)} dk_y dk_x \text{ for } \pm z > 0, \quad (3a)$$

where $k_z^2 = k_0^2 \epsilon_r - k_x^2 - k_y^2$ and p , q , and m are given by,

$$(p, q, m) = \left(k_x / (k_0 \sqrt{\epsilon_r}), k_y / (k_0 \sqrt{\epsilon_r}), \sqrt{1-p^2-q^2} \right), \quad (3b)$$

and k_0 is the wavenumber in free space. The electric and magnetic fields generated by a dipole emitter \mathbf{P} are obtained, respectively, by the Green dyadic representation,

$$\mathbf{E} = \frac{\mu_0 \omega^2}{4\pi \epsilon_r} \tilde{G}^{\pm}(r) \cdot \mathbf{P} \text{ for } \pm z \geq 0, \quad (4a)$$

$$\mathbf{H} = (j\omega \mu_0)^{-1} \nabla \times \mathbf{E}. \quad (4b)$$

We can take the y -axis integration of Eqs. (4a) and (4b) to represent a dipole line source on the y -axis. In Fig. 1(a), a dipole line source is supposed to be aligned along the y -axis in free space. Here, the perfect matched layer (PML) is installed to model unbounded free space, which has necessarily been used in the FMM framework for modeling aperiodic optical structure [12, 16]. This setup is essential for evaluating the side leaky optical power. In Fig. 1(a), the orientation of the dipole in the dipole line source indicates polarization direction. The optical field distribution can be orthogonally decomposed into two separate modes of polarization; transverse electric (TE: $\mathbf{P}_{TE} = (1, 0, 0)$) and transverse magnetic (TM: $\mathbf{P}_{TM} = (0, 0, 1)$) modes. The optical dipole field distributions generated by \mathbf{P}_{TE} and \mathbf{P}_{TM} are presented in the upper and lower parts of Fig. 1(b), respectively. The radiation patterns and corresponding power flows are quite different according to the polarization status of dipole source. In the analysis, the optical field is normalized such that the total radiation power of dipole in free space is to be 2, which is equally divided into the left and right half-infinite spaces.

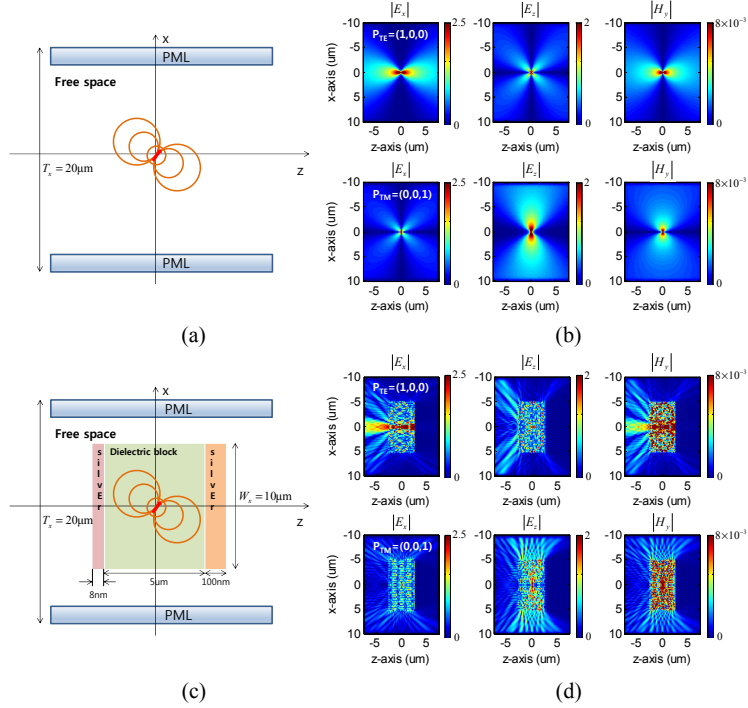


Fig. 1. (a) Dipole emission in free space and (b) vector optical field distributions generated by the dipole emitters with wavelength $\lambda = 532\text{nm}$ and polarizations of $\mathbf{P}_{TE} = (1, 0, 0)$ and $\mathbf{P}_{TM} = (0, 0, 1)$. (c) Dipole emission in a finite-size photonic structure and (d) vector optical field distributions generated by the dipole emitters with respective polarizations.

If the dipole source is embedded inside photonic structure (Fig. 1(c)), complicated optical field distribution can be observed as shown in Fig. 1(d). In FMM, photonic structure is modeled by multi-block structure. The optical field is calculated in each block independently. The optical field in a single block can be further decomposed by the Bloch eigenmodes [11, 12], then the optical field representation takes the linear superposition form of the Bloch eigenmodes with coupling coefficients C_g^\pm and $k_{z,0}^{(g)}$ eigenvalues as

$$\begin{pmatrix} \mathbf{E} \\ \mathbf{H} \end{pmatrix} = \sum_{g=1}^{M^+} C_g^+ \begin{pmatrix} \mathbf{E}^{(g)+} \\ \mathbf{H}^{(g)+} \end{pmatrix} + \sum_{g=1}^{M^-} C_g^- \begin{pmatrix} \mathbf{E}^{(g)-} \\ \mathbf{H}^{(g)-} \end{pmatrix}, \quad (5a)$$

where the Bloch eigenmodes are distinguished into the positive and negative modes with respect to the sign of the imaginary term of the eigenvalue $k_{z,0}$, which are reflected in the superscript \pm in Eq. (5a). g is the mode index, and M^+ and M^- are the number of the positive and negative Bloch eigenmodes. In practical numerical analysis, the numbers of those reciprocal modes are always the same number, $M^+ = M^-$ [12]. The Bloch eigenmodes, $\mathbf{E}^{(g)}$ and $\mathbf{H}^{(g)}$, are represented by the pseudo-Fourier series,

$$\begin{pmatrix} \mathbf{E}^{(g)} \\ \mathbf{H}^{(g)} \end{pmatrix} = e^{j(k_{x,0}x + k_{y,0}y + k_{z,0}^{(g)}z)} \sum_{m=-M}^M \sum_{n=-N}^N \begin{pmatrix} E_{x,m,n}^{(g)} & E_{y,m,n}^{(g)} & E_{z,m,n}^{(g)} \\ H_{x,m,n}^{(g)} & H_{y,m,n}^{(g)} & H_{z,m,n}^{(g)} \end{pmatrix} e^{j\left(\frac{2\pi m}{T_x}x + \frac{2\pi n}{T_y}y\right)}, \quad (5b)$$

where m and n are the indices of the x and y -directional Fourier harmonics, respectively. T_x and T_y are the x and y -directional computational domain periods in FMM. The scattering-matrix method (SMM) enables the boundary condition matching at the border of adjacent single blocks, through which the coupling coefficients in Eq. (5a) are determined [12].

As a sample for analysis, a simple two-dimensional photonic structure is taken as shown in Fig. 1(c), consisting of a thin 8nm thick silver layer, a $5\mu\text{m}$ thick dielectric block, and a 100nm thick silver layer along the z -axis. The lateral length of the target structure is $W_x = 10\mu\text{m}$. We can conduct two-dimensional simulation by setting $N = 0$ and $k_{y,0} = 0$, in this case, the dipole line source is supposed to be on the y -axis. The x -directional computation window width is set to $T_x = 20\mu\text{m}$. The wavelength of the optical field is $\lambda = 532\text{nm}$ and the refractive indices of the dielectric, the left and right silver blocks are set to 1.94, $0.14287 + j3.0518$ and $0.24135 + j2.4805$, respectively. The PML is also used to model the aperiodic structure in unbounded free space. The optical field distributions for the dipole line sources with \mathbf{P}_{TE} and \mathbf{P}_{TM} polarizations are presented in Fig. 1(d), respectively.

As apparent from the field distribution, most of the optical energy of the dipole with polarization, \mathbf{P}_{TE} , is externally radiated to the outside of the structure through the facet $z = -2.5\mu\text{m}$. A small part of the optical energy is guided by total internal reflection and leaks to the outside of the structure through its side-walls. While, the optical field generated by the dipole with polarization, \mathbf{P}_{TM} , is totally different from that of \mathbf{P}_{TE} . It is clearly seen in Fig. 1(d) that the side-wall leaky modes are strongly induced and externally radiative optical energy is greatly reduced rather than the case of \mathbf{P}_{TE} .

In accordance to the modal field representation Eq. (5a), we can derive the modal representation of the Poynting vector \mathbf{S} as

$$\begin{aligned} \mathbf{S} &= \frac{1}{2} \text{Re} \{ \mathbf{E} \times \mathbf{H}^* \} = \frac{1}{2} \text{Re} \left\{ \sum_{g=1}^G |C_g|^2 \mathbf{E}^{(g)} \times \mathbf{H}^{(g)*} \right\} + \frac{1}{2} \text{Re} \left\{ \sum_{g' \neq g}^G C_g C_{g'}^* \mathbf{E}^{(g)} \times \mathbf{H}^{(g')*} \right\} \\ &= \sum_{g=1}^G |C_g|^2 \mathbf{S}_g + \sum_{g' \neq g}^G \mathbf{M}_{g,g'}. \end{aligned} \quad (6)$$

The Poynting vector is obtained by the vector sum of the eigenmode power, $|C_g|^2 \mathbf{S}_g$, and the (g, g') th mixed mode power, $\mathbf{M}_{g,g'}$. If the block is lossy, some portion of the input energy dissipates in the form of ohmic loss, in which case, it is noteworthy that the eigenmodes are no longer orthogonal to each other. In general, the mixed mode power, $\mathbf{M}_{g,g'}$, is a non-zero term and should be taken into account in the power and loss analysis. Let the power distribution of the eigenmodes, $|C_g|^2 \mathbf{S}_g$, be referred to modal power spectrum.

3. Modal power spectrum of a dipole emission field

In this section, the computational formulas of the modal power spectrum are developed. The analysis is applied to reveal the modal structure of the optical power flow from the field distribution in Fig. 1(d). For theoretical completeness, we unfold the theory for three-dimensional structures, but present two-dimensional simulation results for simplicity and clarity of discussion in this paper.

In the modal power spectrum analysis, the Bloch eigenmodes are classified into four characteristic modes: radiative mode, leaky mode, bound mode, and free-space mode. In Fig. 2(a), the numerical scheme for the mode classification is schematically illustrated and the concept of the bound mode and free-space mode are further concretized in Fig. 2(b).

Let us consider the g th eigenmode in the block area specified in $-W_x/2 \leq x \leq W_x/2$, $-W_y/2 \leq y \leq W_y/2$, and $z_- \leq z \leq z_+$. W_x and W_y are the x and y -directional lateral lengths of the structure. z_+ and z_- are the z -axis positions of the right and left boundaries of the block to be analyzed. The input power into the block is defined by the z -directional power flow through the $W_x W_y$ area input facet at $z = z_+$. The input power is divided into the radiative power that is transferred to the output facet at $z = z_-$ with the same area and the leaky power transmitted through the side walls specified at $x = \pm W_x/2$ or $y = \pm W_y/2$ along $z_- \leq z \leq z_+$. The input and radiative powers per unit area are denoted by $P_{input}^{(g)} (z = z_+)$ and $P_{output}^{(g)} (z = z_-)$. The leaky powers per unit area measured through the side walls specified at $z_- \leq z \leq z_+$ and $x = \pm W_x/2$ ($y = \pm W_y/2$) are denoted by $P_x^{(g)} (x = W_x/2)$ ($P_y^{(g)} (y = W_y/2)$), and $P_x^{(g)} (x = -W_x/2)$ ($P_y^{(g)} (y = -W_y/2)$).

According to the relative power ratio comparison, $P_{output}^{(g)} \geq \sum_{x=\pm W_x/2} P_x^{(g)} + \sum_{y=\pm W_y/2} P_y^{(g)}$ or $P_{output}^{(g)} < \sum_{x=\pm W_x/2} P_x^{(g)} + \sum_{y=\pm W_y/2} P_y^{(g)}$, the eigenmodes are classified into the radiative and leaky modes, respectively. The radiative modes contribute to total external radiation from the internal light source. Although the radiative and leaky modes are commonly coupled to the environment, i.e. free space, the side leaky modes are accounted for as the light loss by waveguiding effect. The bound modes are the possible non-radiative modes completely confined inside the photonic structure, uncoupled to free-space. When the Q-factor of the structure is extremely high, optical energy can be stored. The representative bound mode is whispering gallery mode. The bound mode is uncoupled to free-space. Whereas, the free-space mode is uncoupled mode to the photonic structure and propagates through free space. Thus, the internal dipole emission cannot excite the free-space mode. The explained power spectra are formulated mathematically on the basis of the field representation in the FMM, Eq. (5b). The Poynting vector, $\mathbf{S}^{(g)}$, of the g th eigenmode is given by

$$\mathbf{S}^{(g)} = \frac{1}{2} \text{Re} \left\{ \mathbf{E}^{(g)} \times \mathbf{H}^{(g)*} \right\}, \quad (7a)$$

where the cross product term is represented as

$$\mathbf{E}^{(g)} \times \mathbf{H}^{(g)*} = e^{-2\beta^{(g)}z} \sum_{m,n} \sum_{m',n'} \begin{pmatrix} E_{y,m,n}^{(g)} H_{z,m',n'}^{(g)*} - E_{z,m,n}^{(g)} H_{y,m',n'}^{(g)*} \\ E_{z,m,n}^{(g)} H_{x,m',n'}^{(g)*} - E_{x,m,n}^{(g)} H_{z,m',n'}^{(g)*} \\ E_{x,m,n}^{(g)} H_{y,m',n'}^{(g)*} - E_{y,m,n}^{(g)} H_{x,m',n'}^{(g)*} \end{pmatrix} e^{j \left(\frac{2\pi(m-m')}{T_x} x + \frac{2\pi(n-n')}{T_y} y \right)}. \quad (7b)$$

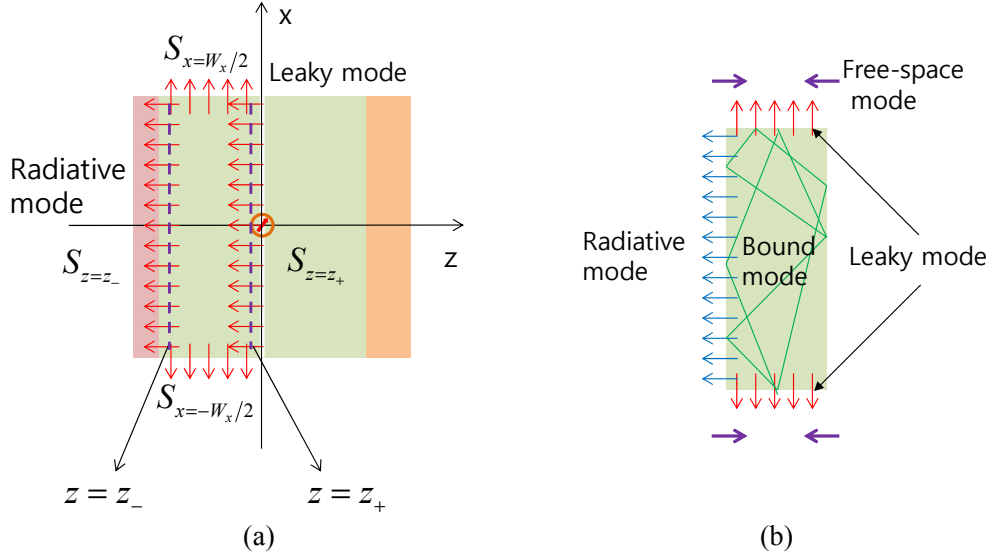


Fig. 2. (a) Modal power spectrum analysis scheme and (b) the classification of optical modes associated with the photonic structure: radiative, leaky, bound, and free-space modes

According to the definition of the input power per unit area, The area-normalized input power is formulated as the area integral of the z-directional Poynting vector normalized by the total integral area $W_x W_y$,

$$P_z^{(g)}(z = z_{\pm}) = \frac{1}{W_x W_y} \int_{-W_x/2}^{W_x/2} \int_{-W_y/2}^{W_y/2} \mathbf{S}^{(g)} \cdot \hat{z} dx dy$$

$$= e^{-2\beta^{(g)} z_{\pm}} \sum_{m=-M}^M \sum_{n=-N}^N \sum_{m'=-M}^M \sum_{n'=-N}^N \frac{1}{2} \text{Re} [E_{x,m,n}^{(g)} H_{y,m',n'}^{(g)*} - E_{y,m,n}^{(g)} H_{x,m',n'}^{(g)*}] \text{sinc} \left(\frac{(m-m')W_x}{T_x} \right) \text{sinc} \left(\frac{(n-n')W_y}{T_y} \right). \quad (8a)$$

The modal power spectrum is defined by the absolute power transmitted by the input facet,

$$Q_z^{(g)} = |C_g|^2 P_z^{(g)} W_x W_y. \quad (8b)$$

The normalized leaky powers of the eigenmode at $x = \pm W_x/2$ and $y = \pm W_y/2$ are calculated, respectively, as

$$P_x^{(g)} \Big|_{x=\pm W_x/2} = \frac{1}{(z_+ - z_-) W_y} \int_{-W_y/2}^{W_y/2} \int_{z_-}^{z_+} \mathbf{S}^{(g)} \cdot \hat{x} dz dy$$

$$= \frac{[e^{-2\beta^{(g)} z_+} - e^{-2\beta^{(g)} z_-}]}{2(z_+ - z_-)(-2\beta^{(g)})} \text{Re} \left(\sum_{m,n} \sum_{m',n'} [E_{y,m,n}^{(g)} H_{z,m',n'}^{(g)*} - E_{z,m,n}^{(g)} H_{y,m',n'}^{(g)*}] e^{j \left(\frac{2\pi(m-n')}{T_x} \left(\frac{\pm W_x}{2} \right) \right)} \right) \text{sinc} \left(\frac{(n-n')W_y}{T_y} \right), \quad (9a)$$

$$P_y^{(g)} \Big|_{y=\pm W_y/2} = \frac{1}{(z_+ - z_-) W_x} \int_{-W_x/2}^{W_x/2} \int_{z_-}^{z_+} \mathbf{S}^{(g)} \cdot \hat{y} dz dy$$

$$= \frac{[e^{-2\beta^{(g)} z_+} - e^{-2\beta^{(g)} z_-}]}{2(z_+ - z_-)(-2\beta^{(g)})} \text{Re} \left(\sum_{m,n} \sum_{m',n'} [E_{z,m,n}^{(g)} H_{x,m',n'}^{(g)*} - E_{x,m,n}^{(g)} H_{z,m',n'}^{(g)*}] e^{j \left(\frac{2\pi(n-n')}{T_y} \left(\frac{\pm W_y}{2} \right) \right)} \right) \text{sinc} \left(\frac{(m-m')W_x}{T_x} \right). \quad (9b)$$

The modal power spectra of those leaky modes are defined, respectively, by

$$Q_x^{(g)} = |C_g|^2 P_x^{(g)}(z_+ - z_-) W_y, \quad (10a)$$

$$Q_y^{(g)} = |C_g|^2 P_y^{(g)}(z_+ - z_-) W_x. \quad (10b)$$

Because the emission source is embedded in the structure, the propagative and leaky modes are excited physically. The open slab structure such as our example structure does not sustain considerable bound modes. Guided waves by the total internal reflection are radiated through the side walls and are thus classified into the leaky mode. The free-space mode is not allowed by the internal emission source. In the analysis, we are focused on the characteristics of the radiative and leaky modes.

Table 1. Modal Power Spectrum of the Dominant Radiative and Leaky Modes

Modal spectrum		P_{TE}	P_{TM}
Radiative mode	Positive (mode index)	1.6881 (51)	0.2169 (64)
	Negative (mode index)	-1.9417 (51)	-0.2787 (64)
Leaky mode	Positive (mode index)	0.0135 (148)	0.0142 (149)
	Negative (mode index)	0.0291 (148)	0.2423 (157)

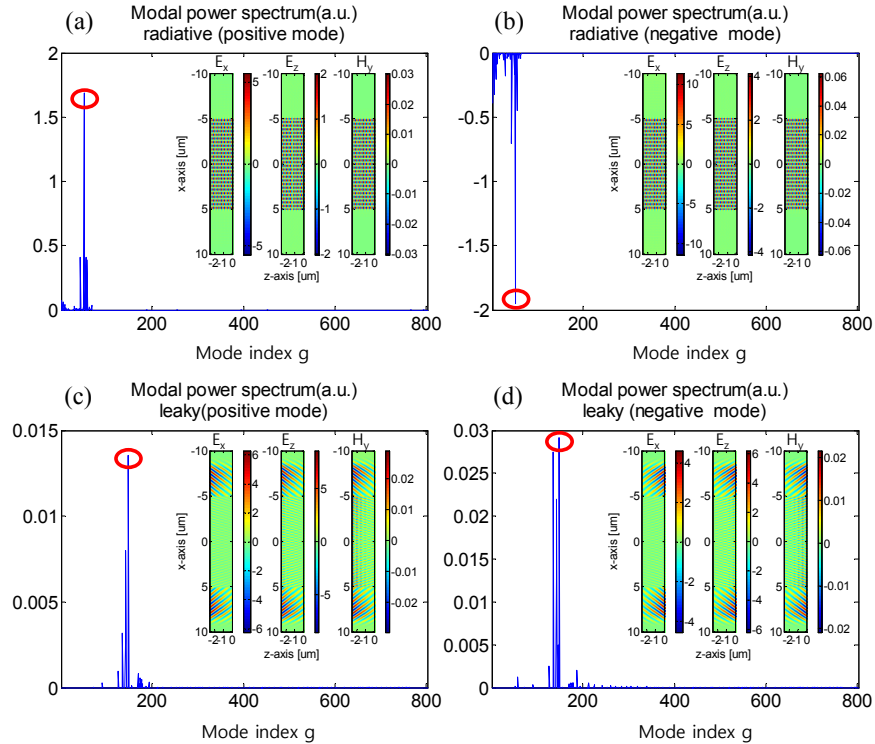


Fig. 3. Modal power spectra of the (a) (positive) and (b) (negative) radiative modes, and (c) (positive) and (d) (negative) leaky modes for $\mathbf{P}_{TE} = (1,0,0)$. The red circles indicate the modes with the highest power selectively and the respective insets present the vector field distributions of the selected Bloch eigenmodes.

Figure 3 shows the modal power spectra of the radiative modes $Q_z^{(g)}$ (Figs. 3(a)-3(b)) and leaky modes $Q_x^{(g)}$ (Figs. 3(c)-3(d)) selectively of the optical field generated in the left part of

the dielectric block by the dipole emitter polarized by \mathbf{P}_{TE} . The power spectra of the positive and negative radiative modes are plotted in Figs. 3(a) and 3(b), respectively. The dominantly excited radiative modes are indicated by the red circles and, in the inset, the field distribution of the dominant eigenmodes are visualized. In Figs. 3(c) and 3(d), the power spectra of the positive and negative leaky modes are plotted with the field visualization of the dominantly excited leaky modes. The power spectrum values of dominantly excited modes are recorded in Table 1. The power spectrum values of the dominant negative modes are greater than those of the positive modes since the position of the emission source is right-sided from the analyzed block. The large positive spectrum values of the negative and positive radiative modes with the same mode index 51, 1.688 and -1.952 , indicate that the strong interference of two modes in the block structure occurs inside the block. The 51st positive and negative modes exist in the form of resonant standing wave in the block. The 51st mode pair is referred to dominant cavity modes. However, we should take into account that the net radiative power of this dominant resonant mode is -0.2636 ($= 1.688 - 1.952$), which is not the highest value. By the same manner, the net leaky power of the dominant mode pair is estimated as 0.0426 ($= 0.0135 + 0.0291$).

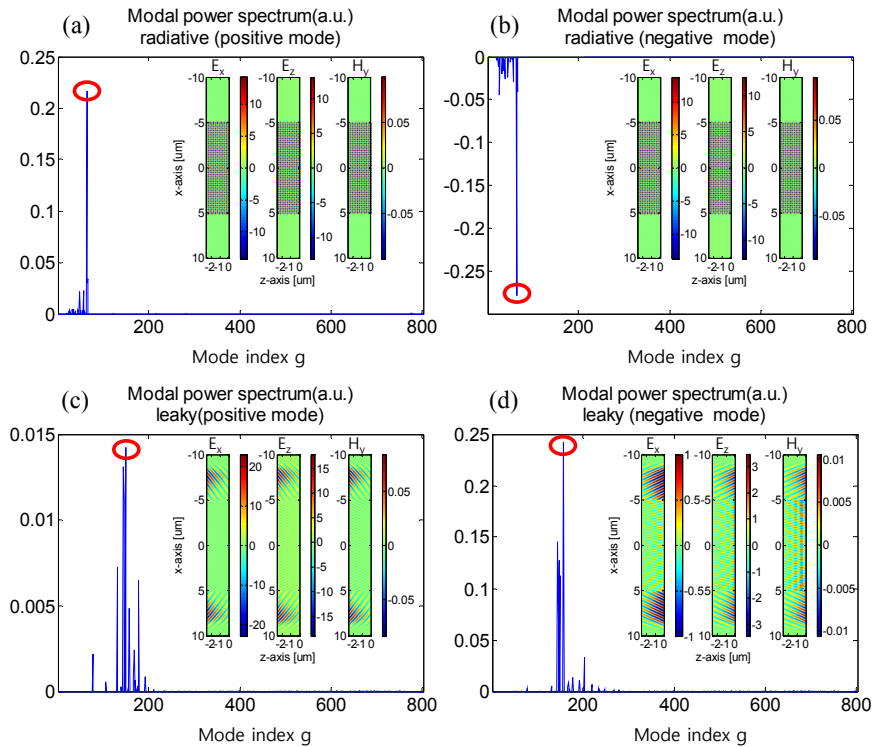


Fig. 4. Modal power spectra of (a) (positive) and (b) (negative) radiative modes, and (c) (positive) and (d) (negative) leaky modes for $\mathbf{P}_{TM} = (0,0,1)$. The red circles indicate the modes with the highest power selectively and the respective insets present the vectorial field distributions of the selected Bloch eigenmodes.

Figure 4 shows the modal power spectra when the dipole polarization is \mathbf{P}_{TM} . The spectrum values of the positive modes are smaller than those of the negative modes similar to the case of polarization \mathbf{P}_{TE} . The net leaky power for the polarization \mathbf{P}_{TE} is 0.2565 ($= 0.0142 + 0.2423$) about six-times larger than 0.0426 in the case of the polarization \mathbf{P}_{TE} . However the

net radiative power $-0.0618 (= 0.2169 - 0.2787)$ is four-times smaller than -0.2636 in the case of the polarization \mathbf{P}_{TE} .

Here, we should note that the dominant cavity mode may not be equal to the mode having maximum radiative power. We need to analyze the net power spectra concerning the highest radiative modes or leaky modes. Considering our sample structure, we see that the structure allows multimode radiation to occur, which is clearly observed in the modal power spectra in Fig. 5. The modal net power spectra of the radiative and leaky modes for the dipole polarization \mathbf{P}_{TE} and \mathbf{P}_{TM} are converted into and comparatively plotted in Figs. 5(a) and 5(b), respectively. The left tables in Figs. 5(a) and 5(b) denote the mode indices of the radiative and leaky modes with highest power spectrum value. It should be noted that, in the case of \mathbf{P}_{TE} , the radiative mode with the highest radiative power (mode index 1) is different from the resonant cavity mode (mode index 51), but the leaky mode (mode index 148) is the same mode as the resonant cavity mode (mode index 148).

The net power values of most eigenmodes are negative values for both polarizations, \mathbf{P}_{TE} and \mathbf{P}_{TM} since the dipole line source is positioned at the right border of the second dielectric block and the optical power flows toward the negative z -axis. However, when the optical wave emitted from the dipole line source that is tightly localized in the origin is reflected at the left boundary of the second block and redirected toward the third block along the positive z -axis, the net power of the Bloch eigenmodes constructing the reflected wave can be positive. The possibility of this occurrence is observed in the modal power spectra in Figs. 5(a) and 5(b), where most eigenmodes including highly excited dominant modes have negative net power values, but some eigenmodes are shown to have positive power values even though the values are relatively small.

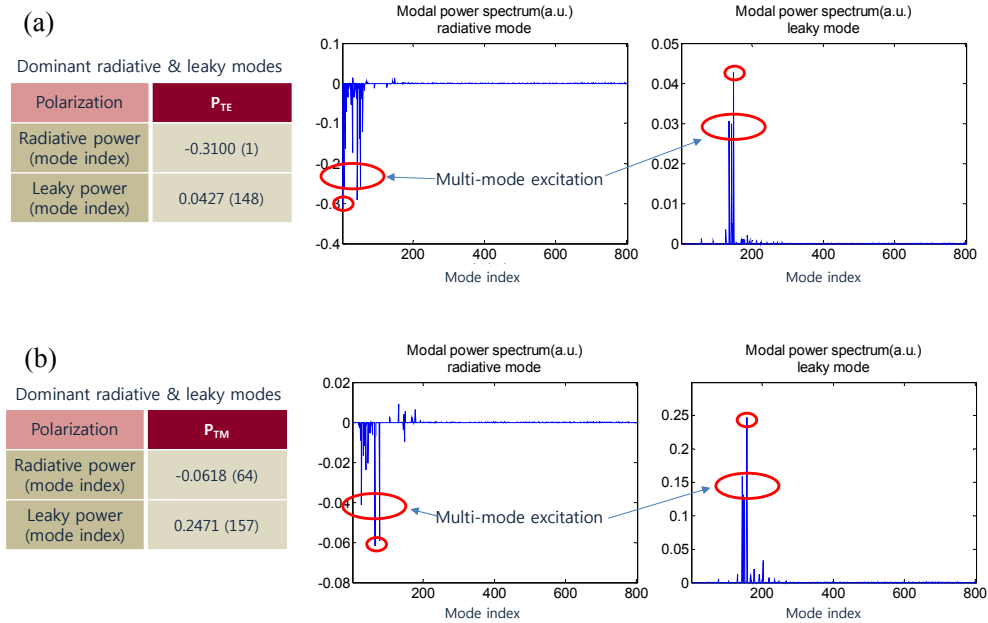


Fig. 5. Modal power spectra of the net radiative modes and net leaky modes for (a) \mathbf{P}_{TE} and for (b) \mathbf{P}_{TM}

4. Quantification of total optical loss and power flow

The main concerns in this analysis are what the contributing portion of high-ranked dominant radiative modes is in the total radiation power and what the contributing portion of high-ranked dominant leaky modes is in the total leaky loss.

Firstly, let us consider the total optical power flow. As discussed in the previous section, the total power transferred by the optical field is decomposed into the part of the eigenmode power and that of the mixed mode power. For lossless medium, we can infer that the mixed mode power would be zero, but in lossy materials such as metals, the mixed mode power might be considerable. Let the total optical field be represented by the linear superposition of the Bloch eigenmodes without separate denotation of the positive and negative modes,

$$\begin{pmatrix} \mathbf{E} \\ \mathbf{H} \end{pmatrix} = \begin{pmatrix} E_x & E_y & E_z \\ H_x & H_y & H_z \end{pmatrix} = e^{j(k_x x + k_y y)} \sum_{m,n} \begin{pmatrix} \sum_g C_g e^{j\beta_g^{(s)} z} E_{x,m,n}^{(s)} & \sum_g C_g e^{j\beta_g^{(s)} z} E_{y,m,n}^{(s)} & \sum_g C_g e^{j\beta_g^{(s)} z} E_{z,m,n}^{(s)} \\ \sum_g C_g e^{j\beta_g^{(s)} z} H_{x,m,n}^{(s)} & \sum_g C_g e^{j\beta_g^{(s)} z} H_{y,m,n}^{(s)} & \sum_g C_g e^{j\beta_g^{(s)} z} H_{z,m,n}^{(s)} \end{pmatrix} e^{j\left(\frac{2\pi m}{T_x} x + \frac{2\pi n}{T_y} y\right)} \quad (11)$$

As similar to the case of modal power spectra, the total power flow is analyzed to be external radiation power, side-leaky loss, and internal loss. The area-normalized total radiative normalized power is obtained by

$$\begin{aligned} P^{total}(z) &= \frac{1}{W_x W_y} \int_{-W_y/2}^{W_y/2} \int_{-W_x/2}^{W_x/2} \frac{1}{2} \text{Re}(\mathbf{E} \times \mathbf{H}^*) \cdot \hat{z} dx dy \\ &= \sum_g C_g C_g^* e^{j\beta_g^{(s)} z} \left(e^{j\beta_g^{(s)} z} \right)^* \frac{1}{2} \text{Re} \left\{ \sum_{m,n,m',n'} [E_{x,m,n}^{(s)} H_{y,m',n'}^{(s)*} - E_{y,m,n}^{(s)} H_{x,m',n'}^{(s)*}] \sin c \left(\frac{(m-m')W_x}{T_x} \right) \sin c \left(\frac{(n-n')W_y}{T_y} \right) \right\}. \end{aligned} \quad (12a)$$

The input and output power per unit area are $P_{input}^{total}(z = z_+)$ and $P_{output}^{total}(z = z_-)$, respectively, in the block analysis indicated in Fig. 2(a). The leaky power measured at $x = \pm W_x/2$ and $y = \pm W_y/2$ are calculated, respectively, as

$$\begin{aligned} P_x \Big|_{x=\frac{\pm W_x}{2}} &= \frac{1}{(z_+ - z_-) W_y} \int_{-W_y/2}^{W_y/2} \int_{-W_x/2}^{W_x/2} \frac{1}{2} \text{Re}(\mathbf{E} \times \mathbf{H}^*) \cdot \hat{x} dz dy \\ &= \frac{1}{(z_+ - z_-)} \sum_g C_g C_g^* \int_{z_-}^{z_+} e^{j\beta_g^{(s)} z} \left(e^{j\beta_g^{(s)} z} \right)^* dz \frac{1}{2} \text{Re} \left\{ \sum_{m,n,m',n'} [E_{y,m,n}^{(s)} H_{x,m',n'}^{(s)*} - E_{x,m,n}^{(s)} H_{y,m',n'}^{(s)*}] e^{j\left(\frac{2\pi(m-n')}{T_x} \left(\frac{\pm W_x}{2}\right)\right)} \sin c \left(\frac{(n-n')W_y}{T_y} \right) \right\}, \end{aligned} \quad (12b)$$

$$\begin{aligned} P_y \Big|_{y=\frac{\pm W_y}{2}} &= \frac{1}{(z_+ - z_-) W_x} \int_{-W_y/2}^{W_y/2} \int_{-W_x/2}^{W_x/2} \frac{1}{2} \text{Re}(\mathbf{E} \times \mathbf{H}^*) \cdot \hat{y} dz dx \\ &= \frac{1}{(z_+ - z_-)} \sum_g C_g C_g^* \int_{z_-}^{z_+} e^{j\beta_g^{(s)} z} \left(e^{j\beta_g^{(s)} z} \right)^* dz \frac{1}{2} \text{Re} \left\{ \sum_{m,n,m',n'} [E_{x,m,n}^{(s)} H_{y,m',n'}^{(s)*} - E_{y,m,n}^{(s)} H_{x,m',n'}^{(s)*}] e^{j\left(\frac{2\pi(m-n')}{T_y} \left(\frac{\pm W_y}{2}\right)\right)} \sin c \left(\frac{(m-m')W_x}{T_x} \right) \right\}. \end{aligned} \quad (12c)$$

The total leaky powers are defined by $Q_x = C_g P_x(z_+ - z_-) W_y$ and $Q_y = C_g P_y(z_+ - z_-) W_x$. The mixed power is represented by the curl of the electric field and magnetic field of two difference photonic modes as addressed by Eq. (6) in section 2. The calculation of the mixed mode power based on Eqs. (12a)-(12c) is time-consuming. In practice, the clever use of the optical modal power spectrum is crucial for efficient computation for total quantification analysis. From the modal spectrum analyzed in the previous section, we can select optical modes with considerable excitation efficiency. The number of selected modes is greatly less than the total number of optical modes derived in the FMM. Most of them are non-excited or

weakly excited optical modes, which are negligible in the calculation of the mixed mode power without loss of accuracy.

The assessment results of the power and energy loss in the four blocks of the target structure are summarized in Table 2. The input energy is split into the radiative and leaky modes and internal loss. The second and third blocks are assumed to be lossless dielectric material, but the considerable loss is counted. This is ascribed to the PML area which is designed to have less-reflection interface and grazing loss. This layer influences the loss mechanism of the leaky modes much greater than that of the radiative mode. Therefore, in the table, we should interpret the radiative power is more close to the true value and the true physical leaky power should be interpreted by the sum of the values of the computed leaky and loss power in Table 2. Considering the first and fourth metal blocks, the computed leaky power is very small, meaning that the leaky waves guided by the surface plasmon channel dissipate inside the structure due to the high ohmic loss of the metal. In this case, the field profile is relatively less influenced by the PML. The computed loss in the table can be interpreted as the physical loss dissipated into the metal layer. Also, as seen in Fig. 1(c), the 1st and 4th silver blocks have 8nm and 100nm thickness, respectively. The transmission rates of optical wave through the 8nm thick block is relatively larger than that through the 100nm thick block. The asymmetric values in the left and right-directional input powers (2.5315 vs. 0.7633 for P_{TE} and 0.6850 vs. 0.5325 for P_{TM}) are due to this asymmetric structure in the analyzed sample.

Table 2. Analysis Result of Total Power and Energy Loss in Total Optical Field

		1st block (Ag)	2nd block	3rd block	4th block (Ag)
$P_{TE} = (1, 0, 0)$	Input	2.2595	2.5315	0.7633	0.4507
	Radiative	1.5382	2.2595	0.4507	0.0108
	Leaky	0.0000	0.1368	0.1440	0.0000
	Loss	0.7213	0.1351	0.1686	0.4399
$P_{TM} = (0, 0, 1)$	Input	0.2499	0.6850	0.5325	0.0791
	Radiative	0.1284	0.2499	0.0791	0.0004
	Leaky	0.0000	0.4132	0.4121	0.0000
	Loss	0.1215	0.0219	0.0413	0.0787

Table 3. Quantitative Analysis of Total Power Flow and Energy Loss

Quantitative analysis	$P_{TE} = (1, 0, 0)$	$P_{TE} = (0, 0, 1)$
Total internal radiation power	3.2948 (= 2.5315 + 0.7633)	1.2175 (= 0.6850 + 0.5325)
Total external radiation	46.7% (= 1.5382/3.2948)	10.55% (= 0.1284/1.2175)
Total leaky loss	17.74% (= 0.5845/3.2948)	72.98% (= 0.8885/1.2175)
Total internal loss	35.2% (= 1.1612/3.2948)	16.4% (= 0.2002/1.2175)

In Table 3, the quantitative analysis result is summarized. For the convenience of understanding the evaluation process, the numbers are colored with respect to types of quantity. The total input powers delivered to the structure for the cases of P_{TE} and P_{TM} are 3.2948(sum of red numbers) and 1.2175(sum of red numbers), respectively. The total internal radiation power of the emitter with P_{TM} is just 37% of that of the dipole emitter with P_{TE} . According to the Purcell effect, the radiation power can be considerably influenced by the distance between the dipole and the metallic block or the axial position of the dipole emitter.

To further discuss about polarization dependency of total radiation power, the polarization-dependent radiation powers with variation in distance variable h are analyzed in Fig. 6. The distance between the dipole emitter and the 8nm silver block shown in Fig. 6(a) is considered a key factor to vary the total radiation power. The left and right directional radiation powers of the dipole are measured and plotted with the distance variable h and polarization of P_{TE} and P_{TM} . As seen in the analysis, the left and right-directional radiation power of dipole is fluctuated with the distance factor h and polarization. When the distance

variable h is set to $h = 2.5\mu\text{m}$, which is indicated by ‘B’ in Fig. 6(b), the power values at that point are equal to the data shown in Table 3. In the case of $h = 1.1\mu\text{m}$, a dramatic change in the left-directional power (to the 2nd block) for \mathbf{P}_{TM} indicated by ‘A’ occurs as clearly observed in Fig. 6(b).

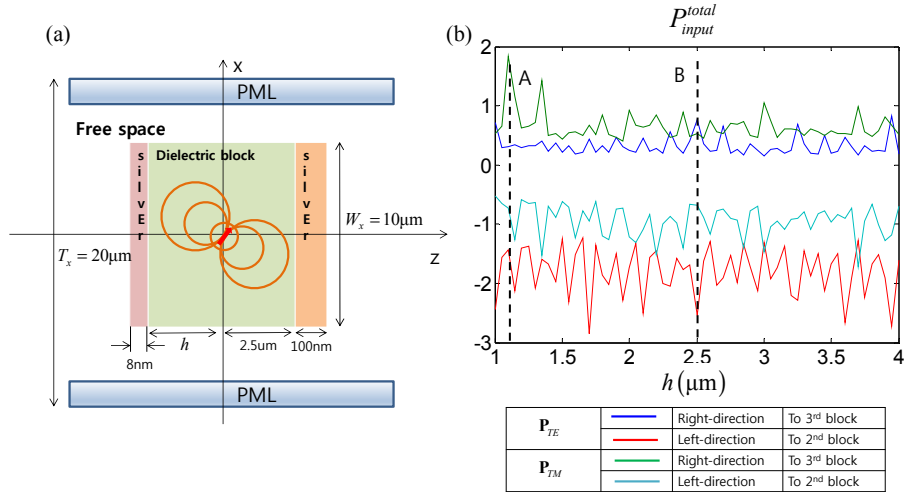


Fig. 6. Total internal radiation powers of the dipole are varied with changing h . (a) h is the distance between the 8nm thick metal block and the dipole line source. (b) Total internal radiation powers of the dipole source with changing h .

Comparing the analysis results of \mathbf{P}_{TE} and \mathbf{P}_{TM} in Tables 2 and 3, we can see that the radiative power, i.e. external radiation power, for \mathbf{P}_{TE} is 1.5383 (blue number) that is about 10 times bigger than that for the polarization \mathbf{P}_{TM} , 0.1579 (blue number). The total external radiation efficiencies are calculated as 46.7% and 10.54%, respectively. On the other hand, the total leaky powers are 0.5925 (sum of green numbers) for \mathbf{P}_{TE} and 1.0936 (sum of green numbers) for \mathbf{P}_{TM} . The leaky loss rates are estimated as 17.98% and 73.02%, respectively. The total internal losses for \mathbf{P}_{TE} and \mathbf{P}_{TM} that are consumed in the metallic blocks are calculated, respectively, as 35% ($= 1.1532/3.2949$) and 16.4% ($= 0.2456/1.4976$) for \mathbf{P}_{TE} and \mathbf{P}_{TM} , respectively. As mentioned above, the analysis on the contributing portion of the dominant modes to the total radiation power and energy loss is of importance for practical applications.

Table 4. Contribution Ratio of Dominant Photonic Modes to Total External Radiation

Modal analysis: the 2nd block	Top 5 modes		Top 10 modes	
	P_{TE}	P_{TM}	P_{TE}	P_{TM}
External radiation	57.6%	67%	85%	85%

For example, we go into details about the second block analyzed in section 2. Considering the multimode radiation characteristics, we try to account the contribution ratios of the top 5 and 10 modes in terms of the external radiation efficiency from Fig. 5. The contribution ratio of the top 5 modes and top 10 modes to the external radiation are evaluated and the result is presented in Table 4. The contribution ratios of the top 5 modes and top 10 modes for \mathbf{P}_{TE} (\mathbf{P}_{TM}) are estimated as quite large 57.6% (67%) and 85% (85%), respectively. The 85% power of top 10 modes is considerable. As seen in Fig. 5, 15% energy is distributed to higher-order eigenmodes as shown in modal power spectra. The sample analyzed in this paper has

considerable thickness, which is intentionally set up for multi-mode excitation. However, most practical devices have very thin layers under 5 μm . In this case, we expect that the number of modes governing dominantly the internal field distribution would be reduced under the number of excited eigenmodes in our sample. It has been revealed that a few dominant modes are mainly contributing the internal power flow and energy loss. The proposed analysis scheme enables us to have insight on the complicated optical radiation phenomena and extract complete information of the dominant modes for further detailed analysis.

5. Conclusion

In conclusion, we have proposed the FMM based quantitative analysis scheme of optical power flow and loss of finite size multiblock structure with a dipole emitter. The analytic representations of the radiative and leaky power flows have been derived and the contribution ratio of a few dominant eigenmodes to external radiation has been analyzed. The description of the analysis scheme is for full three-dimensional modal analysis. The result of full three-dimensional analysis will be announced in near future. We believe that the proposed modal quantitative analysis method can be straightforwardly applied to practical applications such as LEDs, OLEDs, quantum dot (QD) display, and solar cells and provide insight for optimal device design.

Acknowledgment

This research was supported by Samsung Display Co. Ltd., and the Basic Research Program (2010-0022088) through the National Research Foundation of Korea (NRF), funded by the Ministry of Education, Science, and Technology (MEST).